Advances in the calibration of atom probe tomographic reconstruction

Baptiste Gault, Michael P. Moody, Frederic de Geuser, Guy Tsafnat, Alexandre La Fontaine, Leigh T. Stephenson, Daniel Haley, and Simon P. Ringer

View Online   **Export Citation**

ARTICLES YOU MAY BE INTERESTED IN

Atom probe tomography
Review of Scientific Instruments **78**, 031101 (2007); https://doi.org/10.1063/1.2709758

Trajectory overlaps and local magnification in three-dimensional atom probe
Applied Physics Letters **76**, 3127 (2000); https://doi.org/10.1063/1.126545

Design of a femtosecond laser assisted tomographic atom probe
Review of Scientific Instruments **77**, 043705 (2006); https://doi.org/10.1063/1.2194089
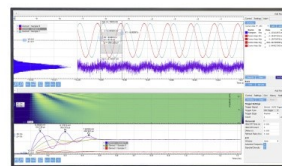
AIP Publishing

Advances in the calibration of atom probe tomographic reconstruction

Baptiste Gault,[1,a)] Michael P. Moody,[1] Frederic de Geuser,[2] Guy Tsafnat,[3] Alexandre La Fontaine,[1] Leigh T. Stephenson,[1] Daniel Haley,[1] and Simon P. Ringer[1]

[1]*Australian Key Centre for Microscopy and Microanalysis, Madsen Building F09, The University of Sydney, NSW 2006, Australia*
[2]*Laboratoire Science et Ingénierie des MAtériaux et Procédés, UMR CNRS 5266, INP Grenoble-BP 46, Domaine Universitaire-101 rue de la Physique 38402, Saint Martin d'Héres, France*
[3]*Centre for Health Informatics, University of New South Wales, Cliffbrook House, 45 Beach St., Coogee NSW 2034, Australia*

Modern wide field-of-view atom probes permit observation of a wide range of crystallographic features that can be used to calibrate the tomographic reconstruction of the analyzed volume. In this study, methodologies to determine values of the geometric parameters involved in the tomographic reconstruction of atom probe data sets are presented and discussed. The influence of the tip to electrode distance and specimen temperature on these parameters is explored. Significantly, their influence is demonstrated to be very limited, indicating a relatively wide regime of experimental parameters space for sound atom probe tomography (APT) experiments. These methods have been used on several specimens and material types, and the results indicate that the reconstruction parameters are specific to each specimen. Finally, it is shown how an accurate calibration of the reconstruction enables improvements to the quality and reliability of the microscopy and microanalysis capabilities of the atom probe. © 2009 American Institute of Physics.
[DOI: 10.1063/1.3068197]

I. INTRODUCTION

In atom probe tomography, individual atoms are removed from the surface of a tip shaped specimen under the effect of a very intense electric field. This is performed by a combination of field-induced ionization and desorption, a process known as field evaporation.[1,2] For most metals, electric field strengths ranging between 10 and 60 V nm^{-1} are required to induce the field evaporation.[3,4] Such electric fields are achieved by subjecting the sharp needle shaped specimen with a radius of curvature, R, less than 100 nm at the apex to a high voltage V, typically several kilovolts. At the tip apex, the field can be related to voltage via[5]

$$F = \frac{V}{k_f R},$$

where k_f is the geometric field factor accounting for the shape of the tip and the influence of the electrostatic environment surrounding the tip inside the instrument. The specimen is generally maintained under ultrahigh vacuum ($<10^{-9}$ Pa) conditions and at cryogenic temperature (below 100 K) to avoid electric field-induced surface diffusion of atoms.

Time-controlled field evaporation is ensured by the application of high voltage (HV) pulses that are usually transmitted via a counterelectrode, which is typically placed at a distance of a few millimeters to a few tens of microns in front of the specimen. The flight time of the ions is recorded by a position-sensitive detector. The flight time enables resolving the chemical identity of each atom by time-of-flight mass spectrometry. The ion impact position is used to determine atomic position at the specimen surface. Indeed, the ions leaving the specimen surface are accelerated by the surrounding electric field and can be considered as quasiradially projected from the tip apex. The field desorption image at the detector contains detailed information on the topography of the tip surface with a magnification that is inversely proportional to the radius of curvature of the tip. By this means, the impact position on the detector directly is directly related to the original position of the atom over the tip surface. A tomographic reconstruction of the probed volume is built up. The result is a three-dimensional (3D) tomographic image of the type and distribution of atoms in a material. The image exhibits a subnanometer resolution, and so atom probe tomography is a high-resolution microscopy and microanalysis technique that reveals the structure and chemistry of materials one atom at a time.

Of fundamental importance in the atom probe technique is the approach to the tomographic reconstruction and this paper focuses on calibrating the parameters that will enable the most accurate reconstruction using the standard reconstruction protocol. Accuracy in the 3D atomic reconstruction requires a detailed understanding of how the ions are projected from the tip onto the detector. The projection of ions has been extensively studied in field ion microscopy (FIM), a technique closely related to atom probe tomography (APT), in which gas atoms are ionized in the vicinity of the tip surface due to the intense electric field.[6–8] Subsequently the gas ions are projected away from the surface of the tip onto a detector, providing an image of the surface. It has been established within this field of research that the actual image formed by the ions can be modeled to a good approximation

a)Author to whom correspondence should be addressed. Electronic mail: b.gault@usy.edu.au.

as a point-projection process.[9–11] The magnification M of the image of a tip with a radius of curvature, R, can be defined as

$$M = \frac{L}{\xi R},$$

where L is the flight distance to the detector and ξ is the image compression factor (ICF), which is assumed to be a constant. The ICF accounts for the modification of field lines in the vicinity of the apex of the tip and the electrostatic environment and ranges between 1 and 2 where these lower and upper bounds represent radial and stereographic projections, respectively.

Previously Bas *et al.* presented a methodology for the tomographic reconstruction in atom probe tomography based on a point-projection model.[12] That method was subject to three key input parameters: the field factor k_f, the ICF ξ, and the detection efficiency of the instrument, η. This work provided a comprehensive treatment of the implementation of a reconstruction algorithm. However, no direct method to accurately determine these three key input parameters was proposed. Conversely, they proposed to adjust the parameters to avoid any curvature of imaged atomic planes and to obtain the right interspacing for this atomic plane family. Previous studies utilizing field ionization undertaken by Sakurai and Muller[13,14] and a combination of FIM and transmission electron microscopy by Hyde *et al.*[15] previously permitted estimations of the field factor. Furthermore, the ICF has been estimated using FIM in the early works of Brandon[9] and Newman *et al.*[16] Its is to be noted that the gas ions in FIM are generated slightly above the surface, and Waugh *et al.* showed that images formed via FIM differ from images formed by the successive impacts of ions that originate from the tip itself, via field evaporation, known as field desorption micrograph.[17,18] Therefore, a FIM-based estimate of the ICF may not be perfectly representative of the image compression value relevant to an atom probe tomography experiment.

It is also noteworthy that the reconstruction procedure of Bas *et al.* was developed for early designs of 3D atom probes which had a very limited field of view.[19] However, as pioneered by Panitz,[20,21] the reduction in the tip to detector ion flight path increased greatly the field of view of the technique. The introduction of the local electrode in the atom probe design provides a field of view of up to ±35° without affecting the elemental sensitivity, the mass resolving power, or the spatial resolution.[22–24] This wide field of view offers the capacity to discern a greater number of prominent crystallographic features in the field desorption image, such as poles and zone lines. An example is provided in Fig. 2 and the observed pattern is somehow similar to the images that can be obtained using field ion or field desorption microscopy. These features, due to trajectory aberrations of the emitted ions,[25–27] reflect the local topography of the tip surface which can be modeled as the intersection of a crystalline lattice with a quasihemispherical cap. However, the exact shape of the tip depends on various experimental parameters, such as the electric field or the temperature.[25,28,29]

Field desorption images, such as those obtained in Fig. 2, provide information that can be applied directly to deter-
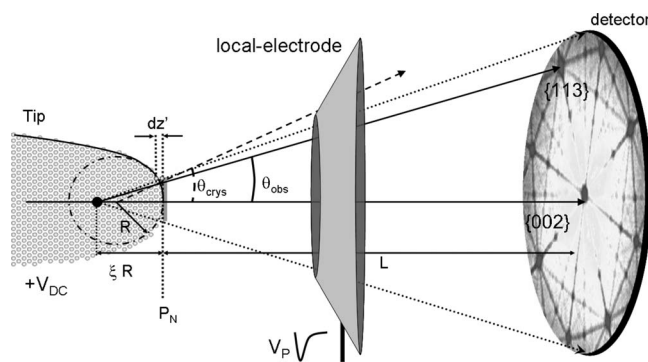

FIG. 1. Experimental setup of a modern atom probe.

mine the key input parameters for tomographic reconstruction in atom probe tomography, as recently discussed in Ref. 30. Building upon this approach, this paper presents a methodology for the measurement of the ICF with significantly improved accuracy through filtering field desorption images using Delaunay triangulation. Additionally, a simplified method for the determination of the field factor is presented. Finally, the effect of some selected variables, such as specimen temperature, local electrode aperture size, and tip to local electrode distance was varied systematically in order to investigate and quantify their respective influence on the projection of the ions and their ultimate effect on the reconstruction. In the sections below, the details of the reconstruction in atom probe tomography are revisited before separately describing our experimental and calculation procedures for the determination of the key input parameters mentioned above.

II. FUNDAMENTALS OF RECONSTRUCTION IN APT

Two main models have been used in APT to describe the projection of ions from the surface of a field emitter onto a position-sensitive detector.[9,31] In both models, the tip is modeled as a hemispherical cap sitting on the top of a truncated cone. Initially, early research showed that the most accurate fit to FIM images was obtained using a projection law $D = k_p \theta$, where D is the distance between these two points on the image and θ is the crystallographic angle formed by the respective directions inside the crystal. In this approach, k_p is a constant for a given instrument and specimen geometry.[16,31]

The second approach is based on a point-projection model as depicted in Fig. 1. In this case the projection origin is located along the axis of the tip at a distance ξR from the tip apex surface. This point corresponds to the intersection of the set of straight lines that relates to the trajectory of the ions between their original position on the surface and their impact position on the detector. This projection of the ions originating from the point positioned at ξR rather than R from the surface is equivalent to considering that the ion trajectories are slightly compressed toward the axis of the tip. Hence the term ξ is generally called ICF. Even though it has been shown that this projection model does not provide the most accurate representation of FIM images,[9,32] it yields,

however, a good approximation, and the generally accepted method for the tomographic reconstruction was developed on this basis.[12]

In the point-projection approach, the magnification M at the detector can be deduced from simple geometrical considerations. Indeed, as defined in Fig. 1, the magnification can be defined by the ratio

$$M = \frac{X_D}{x},$$

where x and X_D are the distance separating two features along the x axis on the tip and detector, respectively. Assuming that the ion is projected straight from a plane P_N normal to the tip apex onto the detector and that the flight path L is much larger than the radius of curvature of the tip, R, the magnification M is more commonly expressed as $M = L/\xi R$. The ICF ξ can be defined by the ratio of the angle θ_{crys} between two crystallographic directions imposed by the theoretical crystalline structure of the material and the angle θ_{obs} observed on the projected image:

$$\xi = \frac{\theta_{crys}}{\theta_{obs}}.$$

Consequently, the ions that are projected from the tip surface follow known trajectories. A univocal relationship exists between each position (x,y) over the tip surface and a position (X_D, Y_D) on the detector. Hence, the original coordinates of the atom can be determined by backprojection from the detector impact position,

$$x = \frac{X_D}{M} \quad \text{and} \quad y = \frac{Y_D}{M}.$$

Assuming a constant field over the surface of the tip, the radius of curvature, R, relating to each detected atom can be directly estimated from the voltage required to induce the evaporation of this atom:

$$R = \frac{V}{k_f F_e},$$

where k_f is the field factor. The evaporation field F_e of the material corresponds to the value of the electric field that lowers the energy barrier that bonds the atom at the surface down to zero. This value is typically taken to be a constant for a given material, and, for the case of an alloy, is generally assumed to assume the value of the alloy's main constituent. Using the equations above, the magnification can be computed for each detected atom and the original coordinates (x,y) at the surface of the specimen can be calculated.

The in-depth (z) component of the position is deduced from the sequence of evaporation. Each atom is assumed to contribute to the depth of the tomographic reconstruction by an increment dz, proportional to its atomic volume divided by the whole observed area over the tip surface. The analyzed area is considered to be the backprojection of the detector onto the tip surface. This area S_a can be simply defined in the plane P_N by

$$S_a = \frac{S_D}{M^2},$$

where S_D is the area of the detector, providing a first approximation of the actual analyzed area (as shown in gray in Fig. 1). The increment in depth also has to account for the limited efficiency. To this end the efficiency parameter η is included in the calculation, effectively meaning that each atom contributes proportionally for more than its own volume toward the in-depth increment. Further, a corrective term dz' is subsequently applied to account for the curvature of the tip and project the atoms back from P_N onto the surface. Finally, the in-depth value can be expressed as

$$z = \left(\sum dz \right) + dz',$$

where

$$dz = \frac{\Omega L^2 k_f^2 F_e^2}{\eta S_D \xi^2 V^2},$$

Ω is the atomic volume and η the detection efficiency, and

$$dz' = R \left(1 - \frac{x^2 + y^2}{R^2} \right) \quad \text{(Ref. 12)}.$$

From the original detector coordinates (X_D, Y_D) and the sequence of evaporation, this global procedure enables the determination of the x, y, and z coordinates of each atom and thus constitutes the tomographic reconstruction. Fundamental to the precision of the final reconstruction is the capacity to accurately define in the three main parameters. The following sections focus on techniques to derive more precise values for k_f and ξ. An approach for the determination of the detector efficiency of the instrument, η, was recently presented[30] and this value ($\sim 57\%$) was assumed constant throughout this work.

III. EXPERIMENTAL

To calibrate the reconstruction parameters, pure aluminum specimens of high purity ($>99.99\%$) metal were prepared using standard electrochemical polishing using standard technique.[33] The specimen tips were analyzed using an Imago LEAP-3000X Si and a LEAP-4, respectively, equipped with 8 and 4 cm delay line detectors at a pulse fraction of 0.25. The specimen temperature was varied between 20 and 150 ± 2 K under ultrahigh vacuum conditions ($<4.5 \times 10^{-9}$ Pa). The average detection rate was also controlled at a rate of 0.025 ions per pulse.

In the first set of experiment, aiming to study the influence of the tip to electrode distance and the electrode aperture diameter on the reconstruction parameters, the position of the tip in front of the local electrode was carefully set using the instrument pulsed laser targeting assembly. The positioning controls of the beam are accurate to within a few microns. The laser beam spot diameter is approximately 10 μm. Prior to the experiment, the beam was first directed onto the local electrode and subsequently moved toward the specimen apex. The beam was then positioned at a specific distance from the end of the electrode. The tip was consequently moved into the beam until the optical diffraction
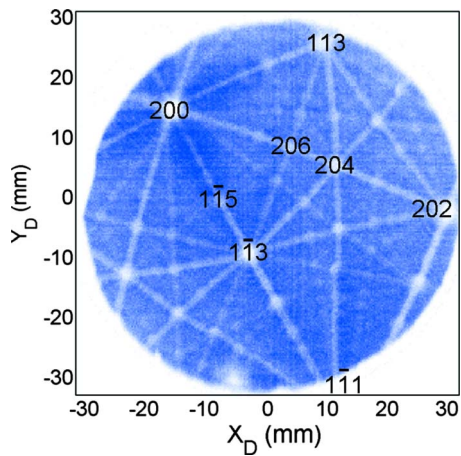
FIG. 2. (Color online) Desorption image of a pure Al specimen analyzed at 40 K, shown as a 2D histogram. The main crystallographic poles have been identified directly on the image.

figure observed was similar for each of the tip to electrode distance. About 1.5×10^6 of atoms were collected for each distance and aperture diameter.

In the second set of experiments the specimen temperature was systematically varied. When the temperature of the specimen was changed, the tip was taken several millimeters away from the electrode. When the specimen reached the new nominal temperature, the tip was carefully brought back to the very same position using the laser-beam-based procedure utilized above. The tip to electrode distance was set at 40 μm and the electrode aperture size was 50 μm. Approximately 2.5×10^6 atoms were collected at each temperature.

In the third series of experiments, the effect of the nature of the specimen on the reconstruction parameters was explored using other various materials. Specimens of several pure metals (W, Ni, Al; different Al-based alloys; a low-alloyed steel; and a doped Si tip on a planar substrate) were investigated. Pure metal and metallic alloy specimens were also prepared by electrochemical polishing.[33] The Sb doped Si tip was part of a commercial presharpened Microtip array prepared by lithographical methods. In these experiments, the tip position had been set so that field desorption image fills up the detector area to limit the variations of k_f with the electrostatic environment as suggested by Ref. 34.

Finally, the measurement of the plane spacing was undertaken by means of Fourier transform[35] or using spatial distribution maps (SDMs).[36,37] SDMs are a real space technique to study the average atomic neighborhoods in the data set. They help quantify the plane interspacing in a material as well as reveal potential order.[36,38]

IV. DETERMINATION OF THE IMAGE COMPRESSION FACTOR

In the case of crystalline materials, the field desorption image formed at the detector can contain detailed crystallographic information such as the poles and zone lines observed in Fig. 2. This contrast arises from trajectory aberrations of the ions due to local field variations where crystallographic directions protrude from the surface of the tip. These regions generally appear as regions of lower hit density on the detector, as apparent in Fig. 2, where the field desorption image is shown in the form of a two-dimensional (2D) histogram of the number of ion hits across the detector area. Variations of density over the surface of the detector are readily observable. Generally, as the projection is close to a stereographic projection, revealing the main symmetries of the crystal, it is possible to identify the crystallographic identity of each pole.

The ICF directly relates to the ratio between crystallographic angles in observed in APT experiment and their theoretical counterparts. Therefore, once the poles have been identified, the ICF can be determined. Indeed, the angle between two directions is fixed by the crystallographic structure and can be calculated using standard relations and knowing the Miller indices of both directions. The experimentally observed angle can be determined in a first approximation by measuring the distance D on the image between two poles and using the approximation

$$\theta_{obs} \approx \arctan \frac{D}{L}.$$

The distance D is simply the lateral separation distance between the centers of the two poles in the field desorption image. The main source of uncertainty in this method originates from the inaccuracy and arbitrariness of the determination of these two points. Hence, a Delaunay triangulation technique method has been developed to accurately and efficiently identify the coordinates of the centers of each individual pole.

The *Delaunay triangulation* of a set of points is a collection of segments such that a circle containing the segment end points does not contain any other points. This method, originally proposed by Delaunay, builds a triangular mesh from a set of individual points.[39] In other terms, the triangles are built such that no point exists inside the circumcircle of any of the triangles. This mesh is the dual structure of the Voronoi tessellation.[40,41] Delaunay triangulation has found application in multiple fields of science, from biology to physics. It is worth noting that it has also recently been implemented to help determine the distribution of distance between precipitates in atom probe tomography data sets.[42] One of the properties inherent to the Delaunay triangulation is that it tends to maximize the minimum angle of all the angles of the triangles. This property makes the area of each triangle representative of the local 2D point density, enabling the detection of low point density regions in a set of points by filtering the triangles of larger area. As crystallographic poles represent low density regions of detector hits in the field desorption image, the triangles in their direct vicinity will possess a significantly larger area. In Fig. 3(a), a subset of 10 000 consecutive detector events was selected from the pure Al data set presented in Fig. 2. A Delaunay triangulation method, similar to that of Barber *et al.*,[43] was applied to these detector positions (X_D, Y_D) as the edges of the triangles. This procedure generated approximately 20 000 triangles displayed in Fig. 3(b) and a magnified view is provided in Fig. 3(c).

The correlation between the large area triangles in Figs. 3(b) and crystallographic features in the field desorption map
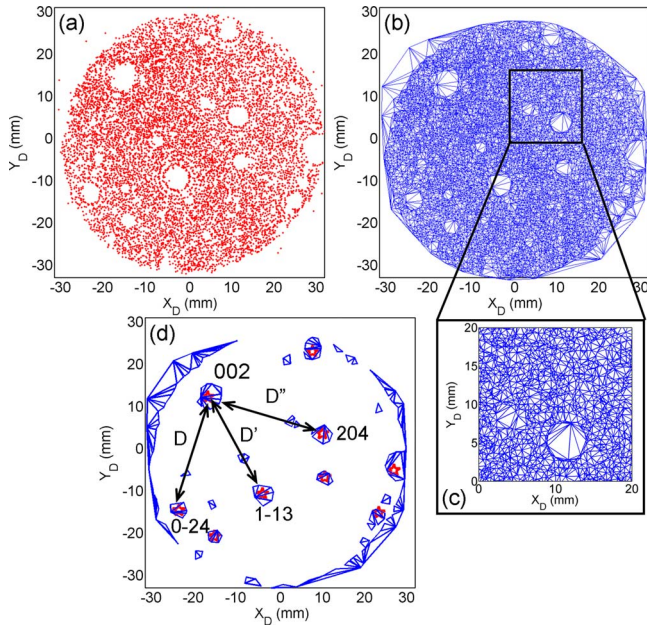
FIG. 3. (Color online) (a) Map of the first 10^4 atom impacts of the same analysis. (b) Result of the Delaunay triangulation. (c) Region of (c) highlighted in black. (d) Triangles filtered in area and centers of the poles identified (red stars).

in Fig. 2 is readily apparent. Subsequently, two filters are applied to the triangulated data. First, triangles that possess an area smaller than threshold value are removed from the data set. Second, all of the remaining large triangles with a centroid beyond some given distance from the center of the analysis, that is slightly less than the radius of the detector, are eliminated from the study. Spurious large triangles on the borders of the images created by surface effects at the edge of the detector are thus removed from the analysis. The remaining triangles are not evenly distributed but instead clustered around specific coordinates associated with the presence of poles, as depicted in Fig. 3(d). Hence, the centroids of two triangles forming a pole will be separated by a distance less than the distance between two triangles associated with two different poles. Therefore, a 2D friends-of-friends search algorithm[44] was then applied to identify clusters of remaining triangles. Similar algorithms have been used extensively in the field of atom probe to detect and characterize atomic clusters.[45–47] The center of each pole was defined as the centroid of all the triangle centroids within a particular cluster. The positions of major crystallographic poles have been automatically identified via implementation of this technique, and these have been annotated as red stars in Fig. 3(d). From a list of the coordinates of the center of the major crystallographic poles it is then possible to compute all the various distances between them. The next and final step of this methodology establishes the crystallographic pole identity. This enables the determination of the ICF by simply dividing the theoretical and experimentally measured interpolar angles and averaging over values measured for all pairs of poles investigated. An important benefit of this approach is the removal of the subjectivity of visual assignment of the exact location of poles, so making the calculations amenable to computation. In the case of the pure Al specimen presented in Fig. 2, an ICF of $\xi=1.55\pm0.15$ was measured using the nine identified poles shown in Fig. 3(d). The statistical standard deviation reflects the spread in values obtained from the measurement of the ICF across the crystallographic poles analyzed.

V. DETERMINATION OF THE FIELD FACTOR

Atomic planes can often be resolved in atom probe tomography.[12,15,48] Once a family of atomic planes $\{hkl\}$ has been identified, the measured interplanar spacing d_{hkl} can be used to calibrate the in-depth dimension of the reconstruction, along the long axis of the tip, as this distance is representative of the fixed crystal structure value $d_{hkl}^{crystal}$. Further, upon re-examination of the reconstruction procedure outlined above, it is apparent that

$$\sum dz \propto \frac{k_f^2 F_e^2}{\xi^2},$$

and Σdz is basically the in-depth coordinate. Therefore, assuming that the electric field is constant and that ξ has been calibrated to a fixed value, the measured plane spacing $d_{hkl}^{measured}$ can be considered as being directly proportional to the square of the field factor:

$$d_{hkl}^{measured} \propto k_f^2.$$

The measurement of the plane spacing in an initial approximate tomographic reconstruction, generated using a first estimated value of the field factor, thus enables the determination a corrected value of the field factor using the relationship

$$\frac{d_{hkl}^{measured}}{d_{hkl}^{crystal}} = \frac{k_f^{2^{initial}}}{k_f^{2^{corrected}}}.$$

In the Al analysis of Fig. 2, the planar interspacing of three independent atomic plane families were measured from a Fourier transform calculated using an algorithm described by Vurpillot *et al.*[35] These values were substituted into the equation above, so providing three independently generated values of $k_f^{2^{corrected}}$. A revised estimation of the field factor value was obtained by averaging over these three independent results. A second reconstruction was then created using this adjusted field factor and the same calibration procedure was reapplied. In general, the error in the measured interspacing after this second step is less than a few percentage. However, the procedure can be applied iteratively to progressively improve the quality of the reconstruction. Here, only one iteration was applied and the plane spacings for the $\{113\}$, $\{115\}$, and $\{117\}$ planes were closer than 2% from their theoretical value, with a determined field factor of $k_f=4.19$.

VI. INFLUENCE OF EXPERIMENTAL CONDITIONS ON RECONSTRUCTION PARAMETERS

Having developed techniques for the independent and precise determination of the reconstruction parameters, k_f and ξ, the focus of this study now turns to an investigation of how they are affected by changes in the experimental conditions commonly encountered in atom probe tomography. The
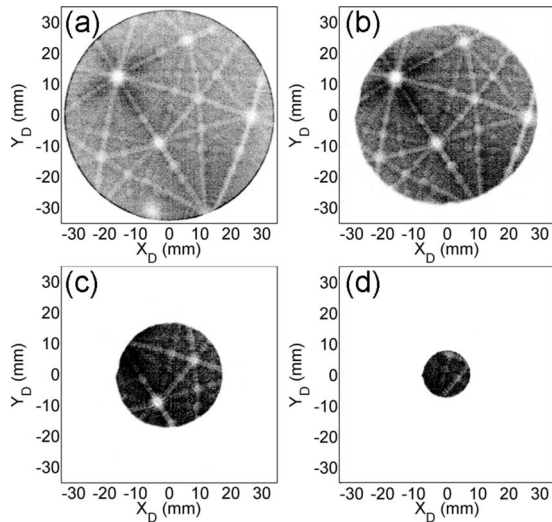
FIG. 4. Successive desorption maps obtained on the same pure aluminum specimen for different tip to electrode distances: (a) 10 μm, (b) 40 μm, (c) 100 μm, and (d) 160 μm.

field factor and ICF were measured as a function of the tip to electrode distance, the electrode diameter, the base temperature of the tip, and the material under study, respectively.

First, a pure Al specimen was analyzed at 40 K. Progressively, the tip was moved further away from the local electrode in a series of successive steps. The tip to electrode distance was carefully measured at each step using the procedure described above. Approximately 1×10^6 atoms were collected at each tip to electrode distance, and a desorption map was plotted to reveal the position of the poles. Examples of the resultant maps are displayed in Fig. 4. As the distance was increased, the analyzed area progressively decreased due to the local electrode acting as a mask to the detector. Interestingly, the relative position of the main poles does not seem to be affected with increasing tip to electrode distance.

Using the same Al specimen, the same procedure varying the tip to local electrode distance was carried out for three local electrodes with significantly different aperture diameters: 50 μm, 85 μm, and 2.5 mm. The latter was used to simulate the behavior of a standard counterelectrode. The ICF was measured at each step and is plotted as a function of the tip to electrode distance in Fig. 5. The image compression remains constant throughout the whole experiment. Within statistical error indicated by the error bars in Fig. 5 the ICF appears independent of both the tip to electrode distance and aperture diameter. An average value of 1.70 ± 0.03 was calculated across all the measurements.

The field desorption maps corresponding to the analyses performed at 20, 40, 80, and 140 K are provided in Fig. 6. Both the ICF and the field factor were subsequently estimated and are plotted as a function of temperature in Figs. 7(a) and 7(b), respectively. Finally, these procedures have been applied to measure k_f and ξ for specimens of various materials. The results of these measurements are provided in Fig. 8.

VII. DISCUSSION

First, it is worth emphasizing that, in the determination of the field factor, the actual parameter that is ultimately
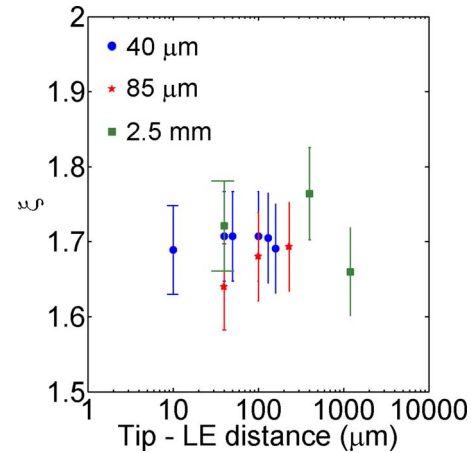

FIG. 5. (Color online) ICF as a function of the tip to local electrode distance for various electrode apertures.

adjusted is not k_f but $k_f F_e$, which is the parameter that effectively appears in the master equations. Throughout this work, F_e was considered as being the calculated value of the evaporation field of Al, which is a strong approximation. However, the fundamental aspects of this work remain valid. The absolute value of the field factor may, however, be different.

The Delaunay triangulation approach developed here proved to be particularly effective in determining the ICF. For example, if major poles, corresponding to low Miller indices in FCC crystals, generally adopt a globally circular shape, higher index poles can show a faceted shape, sometimes much closer to an ellipse. This is readily visible in the simulation of field ion micrographs, as presented by Moore in Ref. 49. The shape of the poles is also highly dependent on the crystal structure, as shown in FIM by Moore and Spink[50] for the {111} W pole. Being based on an assembly of triangles, the pole detection technique involving Delaunay triangulation is not restricted to the detection of circular or even ellipsoidal shapes, which would, for example, be a ma-
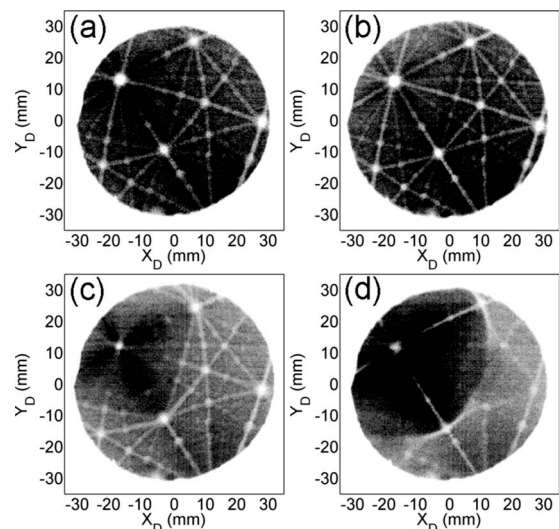

FIG. 6. Successive desorption maps obtained on the same pure aluminum specimen for different specimen temperatures: (a) 20 K, (b) 40 K, (c) 100 K, and (d) 140 K.
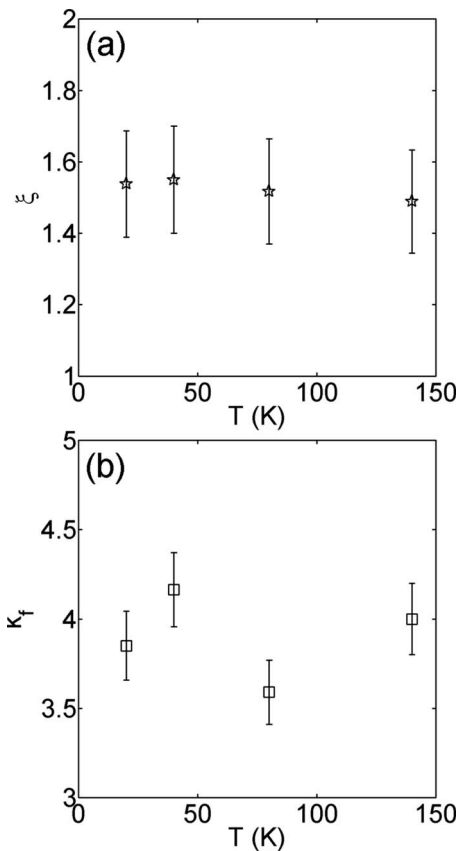
FIG. 7. (a) ICF and (b) field factor as a function of the specimen temperature.

jor limitation of a pole detection procedure based on a Hough transform,[51–53] which is an approach we considered. It is furthermore, much less intensive computationally.

Although this work is focused on independent determination of the image compression and field factors, it is important to note that on top of the statistical errors, instrumentation-related artifacts can induce further variations, particularly to the ICF. For example, as ions travel
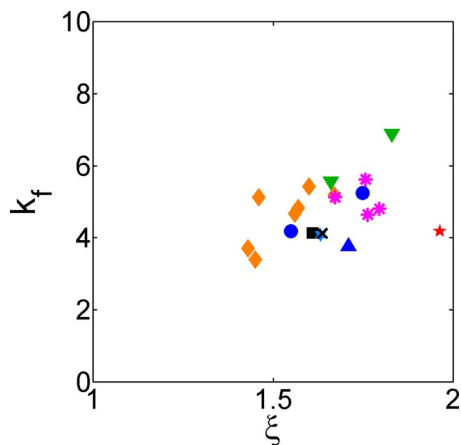

FIG. 8. (Color online) Field factor (k_f) as a function of the ICF (ξ) for several tips and materials: pure aluminum in blue acquired on a 4 cm (triangle up) or a 8 cm (circle) detector, Al–5.6Ag–0.84Cu alloy in orange, Al–3Cu–0.05Sn alloy in magenta, pure Ni in green, pure W in black acquired on a 4 cm (square) or a 8 cm (cross) detector, Sb doped Si on a Microtip array in red, and a high strength low alloy steel in light blue.

between the electrode and the detector, they are also subjected to a voltage applied to bias the microchannel plates used as electron multiplier to enable the detection of the ions. Therefore, their trajectories are unavoidably modified in a way that depends on their mass and on energy. This effect, classically known as postacceleration of the ions, can be detrimental to the positioning capabilities of the technique. As the tip to electrode distance was varied, the voltage required to induce field evaporation of the atoms varies to maintain constant field strength and k_f varies with the distance to the electrode. Further, the transmission of pulses between the electrode and the tip can also be affected and so for a given pulsed voltage, a longer distance can induce a lower pulsed field at the tip surface. Similarly, in the series of experiments investigating the effect of temperature, as the temperature of the tip was increased the evaporation applied voltage consequently decreases. On the basis that field evaporation is a thermally assisted process and the probability of evaporation can be written as a Maxwell–Boltzmann probability, $\exp[-Q(F)/k_BT]$, with $Q(F)$ the field-dependent height of the energy barrier that binds the atom to the surface and k_B and T are, respectively, the Boltzmann constant and the temperature. Hence, the field required to obtain a constant detection rate varies with temperature. The postacceleration artifact induces slight variations in the globally analyzed area, as observed in Fig. 6, which correspond neither to any masking effect nor to any variation of the angular aperture of the instrument, as the very same poles can be observed. This effect was taken into account and a correction of the ion positions was applied in each case keeping the detected surface constant and equivalent to the one observed at 40 K in the measurements of the ICF as a function of the temperature.

The variation in the ICF value between the various experiments on the very same specimen reported here can be explained by several experimental factors. First, the specimen was removed from the vacuum chamber for examination via transmission electron microscopy in between experiments. In this time an oxide layer would form on the surface. When the APT experiments were restarted, this layer was forcibly evaporated from the specimen surface, affecting the nature of the tip. Second, tens of millions of atoms were evaporated between the various experiments, and since the shank angle of the tip was not constant along the tip, the radius of curvature of the tip progressively increased. As it is usual in these circumstances, the voltage was adjusted constantly during the experiments so as to keep the field constant. During the first series of experiments, an average increase in the voltage of 100 V per 1×10^6 detected atoms was required to maintain a constant detection rate constant, while only 15 V per 1×10^6 detected atoms was required in the second series, indicating that the shank angle is much smaller for this part of the specimen, which is consistent with a smaller compression factor of the field lines.

It is worth emphasizing that the evolution of the field desorption images observed as a function of specimen temperature reveals a global change in the topology of the tip surface. These images trace the change in the equilibrium shape of the tip subjected to the electric field. The change

may be explained by the local distribution of the electric field on the surface to variations of the work function and relative evaporation field with the different crystallographic orientations. However, interestingly, despite major changes in the shape, the ICF is not significantly affected. This is a strong indication that the ion trajectories are not affected by microscopic changes in the shape of the tip but more by the mesoscopic scale shape of the specimen shank. Further, considering the results shown in Fig. 8, it may be concluded that there exists no generic set of parameters for a given material or instrument, but rather the parameters vary in between a range already previously defined by FIM.[9,15,16] Our experiments demonstrate that the parameter space is highly dependent on the shape of each individual specimen. This observation is consistent with previous results by Larson *et al.*[54] in which the influence of the shank angle on the field factor was estimated. Further, these results show that, despite the effects of local magnification being intimately linked to the presence of precipitates in the specimen, which are known to have a drastic influence on the accuracy of 3D reconstructions, these methodologies can be applied to estimate the reconstruction parameters, as long as a pole structure and atomic planes can be observed.

Finally, it is critical to the integrity of the final APT reconstruction that ξ and k_f be determined as independently as possible. For example, the depth of the atoms is proportional to the ratio k_f/ξ, and due to this convolution, a range of values that will satisfy this condition exists for these parameters. Consequently, using only one atomic plane family to calibrate the reconstruction only calibrates this ratio and not each parameter separately. However, the curvature correction term implies a dependence on only k_f. Hence, if the value of k_f obtained from this ratio is inaccurate, the curvature correction will be poor, leading to inaccuracy in the angles between the different crystallographic directions and incorrect plane interspacings. In Fig. 9(a), a Fourier transform analysis of a subvolume, highlighted in Fig. 9(b), of the same pure aluminum data reconstructed with the parameters determined as described here is presented. Three sets of reciprocal space vectors are also presented, corresponding to the same data set reconstructed using three independent combinations of k_f and ξ as a comparison. However, the ratio k_f/ξ remains constant across each combination of k_f and ξ. Figure 9(a) highlights the distortion in reciprocal space induced by an arbitrary set of parameters that might ordinarily be considered correct by a calibration procedure that only considers an accurate reconstruction of the {002} plane spacing. Clearly, both the angles and the interspacing for the other atomic plane families are degraded.

VIII. CONCLUSIONS AND OUTLOOKS

In this study, first, strategies were presented to obtain an accurate calibration of the reconstruction parameters for atom probe tomography. Specifically, a methodology was outlined for determination of the ICF and the field factor. Moreover, the variations of these parameters with various experimental conditions were explored.
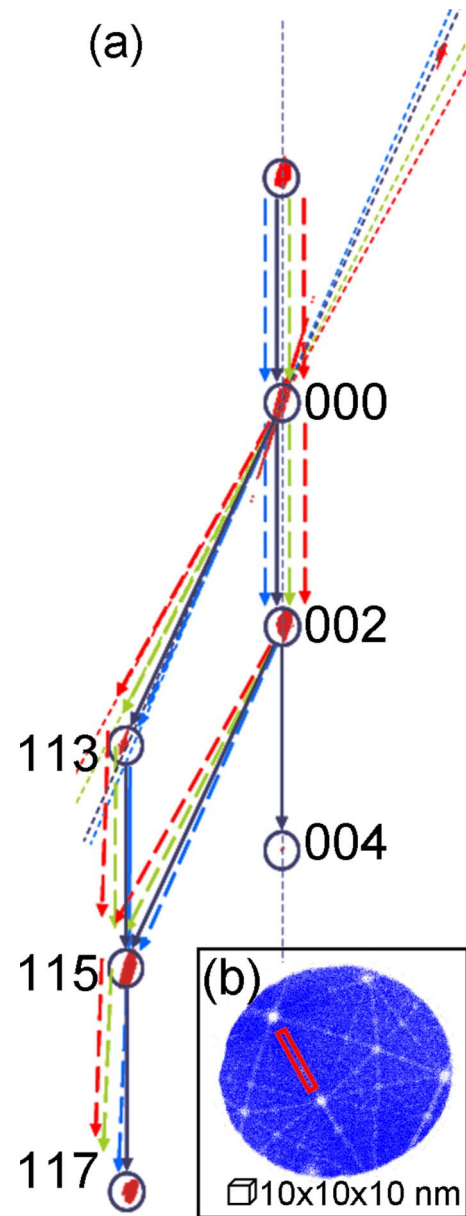

FIG. 9. (Color online) (a) Fourier transform of the subvolume ($3.2 \times 30 \times 3.2$ nm^2) in red in (b). The dark blue lines correspond to the reconstruction (1.55, 4.186). The reciprocal space vectors are represented in dashed line for other couples of reconstruction parameters: (1.20, 3.241) in light green, (1.30, 3.511) in light blue, and (1.80, 4.861) in red. The dotted lines correspond to the angle between the ⟨002⟩ and ⟨113⟩ directions. (b) *XY* map of the same pure Al analysis presented in Fig. 2.

In the first step, a Delaunay triangulation technique coupled to a 2D "friends-to-friends" algorithm was implemented to detect the centers of the poles within the field desorption images, enabling an accurate determination of the ICF ξ. In the present study, the thresholds were manually adjusted until visual satisfaction, and the identity of each pole was also manually set. Work is currently being undertaken to define absolute threshold criteria and to automate the identification of the poles based on symmetry and angle considerations.

Subsequently, assuming that the value of the electric field is known, the field factor k_f was determined by adjusting the atomic plane interspacing measured by a combination

of SDMs and Fourier transform for several atomic plane families. Accurate determination of these parameters should be undertaken for each specimen if possible, as a poor choice of a set of parameters induces distortions of the reconstructed data set.

The ICF is highly dependent on the shape of the tip, much more than on the electrostatic environment of the specimen. This is in good agreement with the independence of the image projection in FIM of the introduction of a counterelectrode a few millimeters away from the tip apex, as discussed by Cerezo *et al.* in Ref. 32. The present study extends this work to the case of a local electrode and using field desorption information, yielding results closer to what is happening in atom probe tomography.[55]

Finally, it is worth noting that the ICF seems to be a constant intimately linked to the global shape and geometry of the specimen and it only varies slightly during an experiment provided that there is no microfracture or that the shape of the tip is initially smooth.

ACKNOWLEDGMENTS

[1]E. W. Muller, Phys. Rev. **102**, 618 (1956).

[2]T. T. Tsong, *Atom Probe Field Ion Microscopy. Field Emission, and Surfaces and Interfaces at Atomic Resolution* (Cambridge University Press, Cambridge, 1990).

[3]T. T. Tsong, Surf. Sci. **70**, 211 (1978).

[4]M. K. Miller, A. Cerezo, M. G. Hetherington, and G. D. W. Smith, *Atom Probe Field Ion Microscopy* (Oxford Science, Oxford/Clarendon, New York, 1996).

[5]H. A. M. Van Eekelen, Surf. Sci. **21**, 21 (1970).

[6]E. W. Muller, Z. Phys. **131**, 136 (1951).

[7]E. W. Muller, Acta Crystallogr. **10**, 823 (1957).

[8]E. W. Muller, Science **149**, 591 (1965).

[9]D. G. Brandon, J. Sci. Instrum. **41**, 373 (1964).

[10]H. N. Southworth and J. M. Walls, Surf. Sci. **75**, 129 (1978).

[11]J. M. Walls and H. N. Southworth, J. Phys. D **12**, 657 (1979).

[12]P. Bas, A. Bostel, B. Deconihout, and D. Blavette, Appl. Surf. Sci. **87–88**, 298 (1995).

[13]T. Sakurai and E. W. Muller, Phys. Rev. Lett. **30**, 532 (1973).

[14]T. Sakurai and E. W. Muller, J. Appl. Phys. **48**, 2618 (1977).

[15]J. M. Hyde, A. Cerezo, R. P. Setna, P. J. Warren, and G. D. W. Smith, Appl. Surf. Sci. **76–77**, 382 (1994).

[16]R. W. Newman, R. C. Sanwald, and J. J. Hren, J. Sci. Instrum. **44**, 828 (1967).

[17]R. J. Walko, and E. W. Muller, Phys. Status Solidi A **9**, K9 (1972).

[18]A. R. Waugh, E. D. Boyes, and M. J. Southon, Nature (London) **253**, 342 (1975).

[19]D. Blavette, B. Deconihout, A. Bostel, J. M. Sarrau, M. Bouet, and A. Menand, Rev. Sci. Instrum. **64**, 2911 (1993).

[20]J. A. Panitz, Rev. Sci. Instrum. **44**, 1034 (1973).

[21]J. A. Panitz, Prog. Surf. Sci. **8**, 219 (1978).

[22]T. F. Kelly, T. T. Gribb, J. D. Olson, R. L. Martens, J. D. Shepard, S. A. Wiener, T. C. Kunicki, R. M. Ulfig, D. R. Lenz, E. M. Strennen, E. Oltman, J. H. Bunton, and D. R. Strait, Microsc. Microanal. **10**, 373 (2004).

[23]S. S. Bajikar, D. J. Larson, T. F. Kelly, and P. P. Camus, Ultramicroscopy **65**, 119 (1996).

[24]T. F. Kelly, P. P. Camus, D. J. Larson, L. M. Holzman, and S. S. Bajikar, Ultramicroscopy **62**, 29 (1996).

[25]F. Vurpillot, A. Bostel, and D. Blavette, J. Microsc. **196**, 332 (1999).

[26]F. Vurpillot, A. Bostel, E. Cadel, and D. Blavette, Ultramicroscopy **84**, 213 (2000).

[27]F. Vurpillot, A. Bostel, A. Menand, and D. Blavette, Eur. Phys. J.: Appl. Phys. **6**, 217 (1999).

[28]E. W. Muller, J. Appl. Phys. **28**, 1 (1957).

[29]K. D. Rendulic and E. W. Muller, J. Appl. Phys. **38**, 2070 (1967).

[30]B. Gault, F. de Geuser, L. T. Stephenson, M. P. Moody, B. C. Muddle, and S. P. Ringer, Microsc. Microanal. **14**, 296 (2008).

[31]T. J. Wilkes, G. D. W. Smith, and D. A. Smith, Metallography **7**, 403 (1974).

[32]A. Cerezo, P. J. Warren, and G. D. W. Smith, Ultramicroscopy **79**, 251 (1999).

[33]M. K. Miller and G. D. W. Smith, *Atom Probe Microanalysis: Principles and Applications to Materials Problems* (Materials Research Society, Pittsburg, PA, 1989).

[34]M. K. Miller and K. F. Russell, Surf. Interface Anal. **39**, 262 (2007).

[35]F. Vurpillot, G. da Costa, A. Menand, and D. Blavette, J. Microsc. **203**, 295 (2001).

[36]B. P. Geiser, T. F. Kelly, D. J. Larson, J. Schneir, and J. P. Roberts, Microsc. Microanal. **13**, 437 (2007).

[37]M. P. Moody, B. Gault, L. T. Stephenson, D. Haley, and S. P. Ringer, Ultramicroscopy (2009) (to be published).

[38]T. Boll, T. Al Kassab, Y. Yuan, and Z. G. Liu, Ultramicroscopy **107**, 796 (2007).

[39]B. Delaunay, Otdelenie Matematicheskikh i Estestvennykh Nauk **7**, 793 (1934).

[40]G. Voronoi, J. Reine Angew. Math. **133**, 97 (1907).

[41]R. Dyer, H. Zhang, and T. Moller, in *Proceedings of the 2007 ACM Symposium on Solid and Physical Modeling* (ACM, Beijing, China, 2007).

[42]R. A. Karnesky, D. Isheim, and D. N. Seidman, Appl. Phys. Lett. **91**, 013111 (2007).

[43]C. B. Barber, D. P. Dobkin, and H. Huhdanpaa, ACM Trans. Math. Softw. **22**, 469 (1996).

[44]K. Florek, J. Lukaszewicz, J. Perkul, H. Steinhaus, and S. Zubrzycki, Colloq. Math. **2**, 282 (1951).

[45]M. K. Miller and E. A. Kenik, Microsc. Microanal. **10**, 336 (2004).

[46]A. Heinrich, T. Al-Kassab, and R. Kirchheim, Mater. Sci. Eng., A **353**, 92 (2003).

[47]L. T. Stephenson, M. P. Moody, P. V. Liddicoat, and S. P. Ringer, Microsc. Microanal. **13**, 448 (2007).

[48]P. J. Warren, A. Cerezo, and G. D. W. Smith, Ultramicroscopy **73**, 261 (1998).

[49]A. J. W. Moore, J. Phys. Chem. Solids **23**, 907 (1962).

[50]A. J. W. Moore and J. A. Spink, Surf. Sci. **12**, 479 (1968).

[51]D. H. Ballard, Pattern Recogn. **13**, 111 (1981).

[52]P. V. C. Hough, U.S. Patent No. 3,069,654, (December 18, 1962).

[53]J. Illingworth and J. Kittler, Comput. Vis. Graph. Image Process. **44**, 87 (1988).

[54]D. J. Larson, K. F. Russell, and M. K. Miller, Microsc. Microanal. **5**, 930 (1999).

[55]A. R. Waugh, E. D. Boyes, and M. J. Southon, Surf. Sci. **61**, 109 (1976).